Physics in Medicine & Biology

PAPER

Inter-crystal scattering recovery of light-sharing PET detectors using convolutional neural networks

To cite this article: Seungeun Lee and Jae Sung Lee 2021 *Phys. Med. Biol.* **66** 185004

IOP Publishing Phys. Med. Biol. 66 (2021) 185004 https://doi.org/10.1088/1361-6560/ac215d

Physics in Medicine & Biology

IPEM Institute of Physics and Engineering in Medicine

CrossMark

RECEIVED
24 February 2021

REVISED
19 August 2021

ACCEPTED FOR PUBLICATION
26 August 2021

PUBLISHED
9 September 2021

PAPER

Inter-crystal scattering recovery of light-sharing PET detectors using convolutional neural networks

Seungeun Lee[1,2] **and Jae Sung Lee**[1,3,*]

[1] Department of Nuclear Medicine, Seoul National University, Seoul, 03080, Republic of Korea
[2] Department of Biomedical Sciences, Seoul National University, Seoul, 03080, Republic of Korea
[3] Brightonix Imaging Inc., Seoul, 04782, Republic of Korea
[*] Author to whom any correspondence should be addressed.

E-mail: jaes@snu.ac.kr

Keywords: inter-crystal scattering, convolutional neural network, PET

Abstract

Inter-crystal scattering (ICS) is a type of Compton scattering of photons from one crystal to adjacent crystals and causes inaccurate assignment of the annihilation photon interaction position in positron emission tomography (PET). Because ICS frequently occurs in highly light-shared PET detectors, its recovery is crucial for the spatial resolution improvement. In this study, we propose two different convolutional neural networks (CNNs) for ICS recovery, exploiting the good pattern recognition ability of CNN techniques. Using the signal distribution of a photosensor array as input, one network estimates the energy deposition in each crystal (ICS-eNet) and another network chooses the first-interacted crystal (ICS-cNet). We performed GATE Monte Carlo simulations with optical photon tracking to test PET detectors comprising different crystal arrays (8×8 to 21×21) with lengths of 20 mm and the same photosensor array (3 mm 8×8 array) covering an area of 25.8×25.8 mm^2. For each detector design, we trained ICS-eNet and ICS-cNet and evaluated their respective performance. ICS-eNet accurately identified whether the events were ICS (accuracy $> 90\%$) and selected interacted crystals (accuracy $> 60\%$) with appropriate energy estimation performance ($R^2 > 0.7$) in the 8×8, 12×12, and 16×16 arrays. ICS-cNet also exhibited satisfactory performance, which was less dependent on the crystal-to-sensor ratio, with an accuracy enhancement that exceeds 10% in selecting the first-interacted crystal and a reduction in error distances compared when no recovery was applied. Both ICS-eNet and ICS-cNet exhibited consistent performances under various optical property settings of the crystals. For spatial resolution measurements in PET rings, both networks achieved significant enhancements particularly for highly pixelated arrays. We also discuss approaches for training the networks in an actual experimental setup. This proof-of-concept study demonstrated the feasibility of CNNs for ICS recovery in various light-sharing designs to efficiently improve the spatial resolution of PET in various applications.

1. Introduction

Positron emission tomography (PET) systems visualize *in vivo* distributions of positron-emitting radiopharmaceuticals by reconstructing tomographic images from the lines-of-response (LORs) measured along back-to-back 511 keV annihilation photon pairs (Phelps 2000, Ametamey *et al* 2008). The accurate estimation of the annihilation photon interaction positions within the PET detectors is directly related to the accurate drawing of LORs, which is crucial for improving the reliability of PET measurements. A traditional method for achieving a high resolution in PET is using pixelated scintillation crystals (Kwon *et al* 2011, Yoon *et al* 2012, Grant *et al* 2016, Cherry *et al* 2018, Van Sluis *et al* 2019, Son *et al* 2020). Recently, monolithic crystals have achieved reasonable positioning accuracies (Gonzalez-Montoro *et al* 2017, Borghi *et al* 2018, Krishnamoorthy *et al* 2018). The spatial blurring in the peripheral region of the PET field-of-view can be reduced with the ability

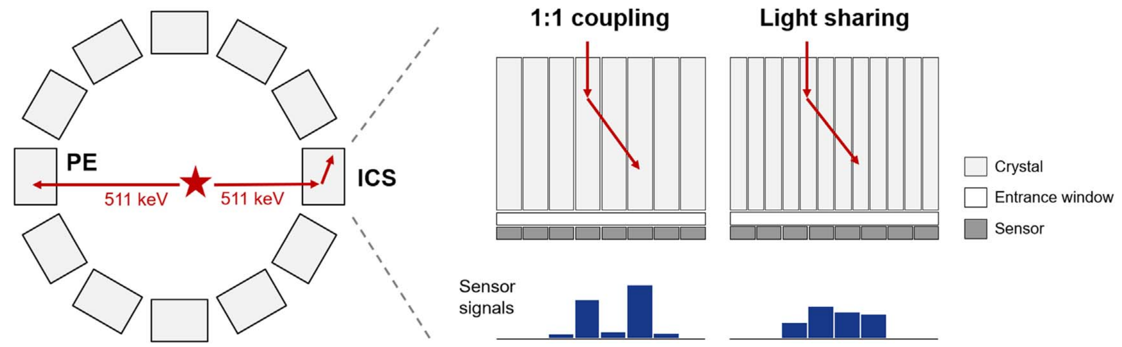

Figure 1. Schematic of PE and ICS of 511 keV annihilation photons in PET detectors. Although the sensor signals are individually read out, the interacted crystals and respective energy depositions of the ICS events are not evident in the light-sharing detectors.

to estimate the depth-of-interactions within the crystals (Yamamoto and Ishibashi 1998, Ito *et al* 2011, 2013, Lee *et al* 2017, Schmidt *et al* 2018, Akamatsu *et al* 2019).

The positioning accuracy of PET, however, is degraded by the physical nature of photon interactions with matter. A major degradation factor is inter-crystal scattering (ICS). ICS involves one or more Compton scatterings of an incident photon in different crystals. In contrast to photoelectric (PE) absorption, where a photon deposits its entire energy in a single interaction position, ICS results in the incorrect assignment of the LOR because energy deposition occurs in more than one crystal (figure 1). Consequently, ICS worsens the spatial resolution of PET. ICS accounts for a significant portion of the detection events in PET measurements, given that for 511 keV photons, the cross-sections of Compton scattering in typical crystal materials are larger than those of PE (Berger *et al* 2010). To overcome the PET performance degradation caused by ICS, several research groups have studied the effects of ICS on PET performance (Miyaoka and Lewellen 2000, Ritzer *et al* 2017, Hsu *et al* 2019, Teimoorisichani and Goertzen 2019, Zhang *et al* 2019, Lee *et al* 2020) and developed algorithms that identify and recover ICS events using energy deposition and interaction position information (Comanor *et al* 1996, Shao *et al* 1996, Rafecas *et al* 2003, Pratx and Levin 2009, Gillam *et al* 2014, Lage *et al* 2015, Abbaszadeh *et al* 2018, Lee *et al* 2018, Surti and Karp 2018).

Identifying and recovering ICS events is more challenging in a light-sharing PET detector than in a 1:1 coupled detector. If each photosensor is coupled to only one crystal (i.e. 1:1 coupling), the energy deposited in the individual crystals can be easily measured (figure 1). Moreover, ICS in a 1:1 coupling detector design can be identified using electronic circuits based on individual (Ota *et al* 2016) or multiplexed (Park and Lee 2020) signal readouts. However, the 1:1 coupling detector has limited design flexibility because the crystal and photosensor pitches must be identical. To achieve a sub-millimeter spatial resolution with small crystals, a light-sharing detector design must be designed, in which a photosensor is coupled with more than one crystal. Consequently, the interacted crystals and their respective energy depositions are not evident under ICS in the light-sharing detectors. A typical method for identifying the interacted crystals in light-sharing designs is to use a two-dimensional (2D) floodmap, which is generated using multiplexing circuits or Anger logic (Du *et al* 2013, Ko *et al* 2013, Park *et al* 2017), as shown in figure 3. While PE events occurring in each crystal appear as peaks in the floodmap, ICS events are broadly distributed as superpositions of crystal positions weighted by signal amplitudes.

To perform ICS recovery in light-sharing PET detectors, we propose convolutional neural network (CNN) models that estimate event-by-event energy depositions or determine the first-interacted crystals. The CNN is a well-established technique for recognizing patterns in images (Lecun *et al* 2015) as well as outperforming traditional numerical and statistical methods in various medical image processing tasks (Hwang *et al* 2018, Park *et al* 2018, Hegazy *et al* 2019, Lee *et al* 2019, Gong *et al* 2020, Khouani *et al* 2020, Lee 2020). With regard to ICS recovery, artificial neural networks are expected to have advantages in integrating Compton scattering kinematics, Klein–Nishina probabilities, optical photon transport, and detector responses of ICS events, with an additional benefit in the reduction of computational burden. Regarding the distribution of signal amplitudes from the photosensor array as a 2D image, we applied a CNN rather than simple perceptron learning, to fully utilize the 2D information to extract the features of energy depositions due to Compton scatterings. With the rapid advancement of technology to handle numerous readout channels and enhance the detector performance, the development of PET detectors based on individual signal readout, rather than multiplexed signal readout, is increasing. Therefore, this study assumed that signals from the silicon photomultiplier array were individually measured.

Table 1. Geometries of the tested crystal arrays.

Crystal array	CSR	Crystal pitch (mm)	Crystal width (mm)
8 × 8	1:1	3.2	3.0
12 × 12	1.5:1	2.1	2.0
16 × 16	2:1	1.6	1.5
21 × 21	2.625:1	1.2	1.08

We conducted a proof-of-concept study to evaluate the feasibility of the proposed CNN-based ICS recovery methods for various designs of PET detectors through Monte Carlo simulations. Then, we evaluated the methods by studying their ability to identify the interacted crystals and energy depositions of the photon interactions. The effects of the proposed methods on the spatial resolution of prototype PET rings were also investigated.

2. Materials and methods

2.1. Detector designs

The tested LSO (Lu_2SiO_5, density = 7.4 g cm^{-3}, refractive index = 1.82) crystal arrays had similar overall block sizes, but with different crystal pitches or crystal-to-sensor ratios (CSRs), as shown in table 1. An 8 × 8 crystal array was used for a 1:1 coupled detector with a crystal size suitable for whole-body imaging. Other detectors featured light-sharing designs suitable for imaging smaller objects, such as human organs (2.1 and 1.6 mm pitches) and small-animals (1.2 mm pitch). The crystal length was 20 mm in all cases. Each crystal array was coupled with the same photosensor array. The 25.8 × 25.8 × 1.5 mm^3 glass entrance window (density = 2.5 g cm^{-3}, refractive index = 1.5) of the photosensor array served as a light guide to distribute the optical photons received from the crystals to photosensitive pixels. A photosensor with a total size of 25.6 × 25.6 mm^2 was formed by an 8 × 8 array of 3 × 3 mm^2 photosensitive pixels in a 3.2 mm pitch as illustrated in figure 1.

2.2. Simulation setup

The entire dataset was acquired via a GATE v8.2 Monte Carlo simulation (Jan *et al* 2004) and an optical photon simulation based on the UNIFIED model (Levin and Moisan 1996). The crystal surfaces were polished with the sigma-alpha value set to 0.1°, where the sigma-alpha in the UNIFIED model is defined as the FWHM in the angular distribution of the micro-facet surface relative to the macro-surface. The surfaces (except for the side coupled to the photosensor) were wrapped with a diffusive reflector with 98% reflectivity. The photodetection efficiency of the photosensitive area was 40%, whereas the light yield of the LSO crystal was 26 000 MeV^{-1} with 9% intrinsic energy resolution at 511 keV. In this study, we did not model the lutetium background of the crystal or the noise of the photosensors.

A 25.8 × 25.8 mm^2 square-shaped uniform planar source was placed 10 cm above the top face of the crystal array. The source emitted 511 keV photons perpendicular to the crystals. For every simulation setup throughout this study, the number of source emissions was set to acquire approximately 20 000 first-interacted events per crystal. An energy threshold of 400 keV was applied to the total energy deposited on the crystal array. For each event, we recorded the signal amplitudes of the sensors, energy depositions in the crystals, and sequence of interactions. To neglect intra-crystal scatterings, which accompany one or more Compton scatterings within a single crystal, we summed the energy depositions within each crystal.

Prior to CNN implementations, we evaluated the occurrence rates of each event type by classifying the events according to the number of interacted crystals for 511 keV photons. The events with only one crystal interaction were regarded as PE, and those with more than one crystal interaction were regarded as ICS.

2.2.1. *Effect of optical parameters*

We investigated the individual effects of three different optical properties on the performances of the networks. A single optical simulation parameter was varied, while other parameters were fixed:

(1) Light yield (26 000 MeV-1): 25%, 50%, 100%, and 200%.

(2) Intrinsic energy resolution (9% at 511 keV): 50%, 100%, 150%, and 200%.

(3) Reflectivity (98%): 25%, 50%, 75%, and 100%.

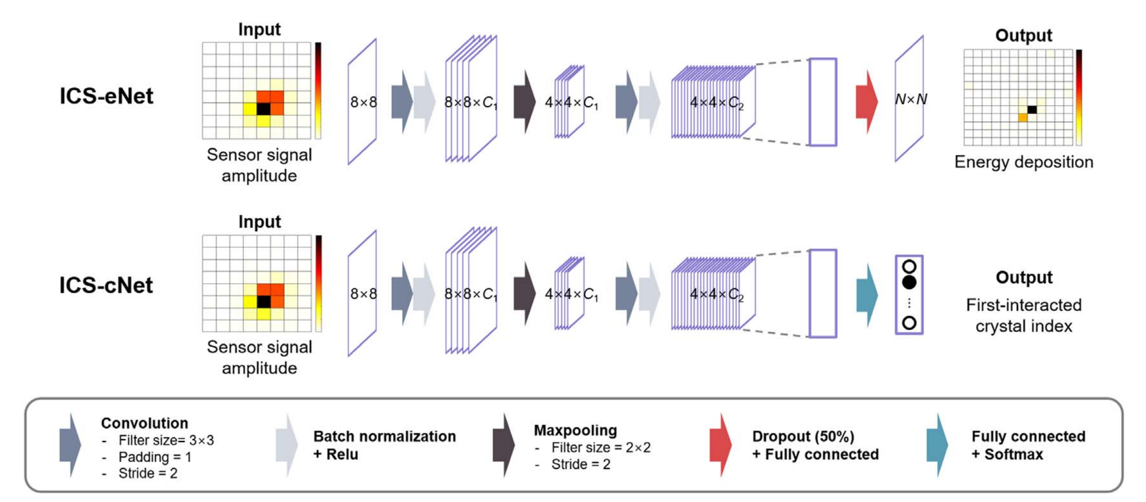

Figure 2. Structures of ICS-eNet and ICS-cNet. C_1 and C_2 denote the numbers of channels in the respective convolution layers to be optimized.

The light yield and intrinsic energy resolution were modified for the LSO material properties, while the reflectivity was modified for the surface settings of the crystal elements. A 12 × 12 array was evaluated as the representative design. Other details of the simulation setup and the training procedures were identical to those reported in sections 2.2 and 2.3.

2.3. CNN structures

We modeled two different networks, namely ICS-eNet and ICS-cNet, that use an 8 × 8 distribution of the sensor signals as a 2D input (figure 2). ICS-eNet was designed to identify event types and estimate energy depositions in individual crystals. The application of ICS-eNet is not a complete recovery process; however, its output can be used to apply existing ICS recovery algorithms mentioned in section 1. ICS-cNet directly selects the crystal where the photon first undergoes Compton scattering. Both CNNs consisted of two convolution layers with one 2 × 2 max-pooling layer between them. The sizes of the filter and stride in the convolution layers were 3 × 3 and 2 × 2, respectively. Each convolution layer was followed by batch normalization and a rectifying linear unit layer. In ICS-eNet, a dropout layer with a 50% dropout probability and a fully connected layer were added to estimate the $N \times N$ distribution of the energy deposition in each crystal as an output layer (where N denotes the number of crystals). ICS-eNet was trained using the Adam optimizer and root-mean-square error (RMSE) loss. Because ICS-cNet is a classification process, a fully connected layer and a softmax layer were incorporated to determine the index of the first-interacted crystal. ICS-cNet was trained using the Adam optimizer and cross-entropy loss.

The dataset was divided into training and validation sets (85% and 15%, respectively). The number of channels in each layer (C_1 and C_2 in figure 2) was optimized for each detector design. We used MATLAB Deep Learning Toolbox R2020b for the entire learning procedure.

2.4. Evaluation

2.4.1. ICS-eNet

As a preprocessing step in the recovery process, the events were first classified as PE or ICS using an algorithm together with the output of ICS-eNet. For each event, we sorted the $N \times N$ output of the estimated energy depositions and then selected the crystals with the largest (E_1) and second largest (E_2) energies. If E_1/E_2 was greater than a certain threshold, the event was classified as PE and the crystal with E_1 was selected as the interacted crystal because the number of interacted crystals is expected to be 1 in PE events. Otherwise, the event was classified as ICS, and crystals with E_1 and E_2 were selected as the interacted crystals. The threshold was set where the E_1/E_2 histogram of PE and ICS was divided with minimal error. We defined the event classification accuracy as follows:

$$\frac{\#(\text{PE classified as PE}) \; + \#(\text{ICS classified as ICS})}{\#(\text{Total events})} \times 100\%.$$

After classification using the E_1/E_2 algorithm, we measured the crystal selection accuracies for PE and ICS individually as follows:

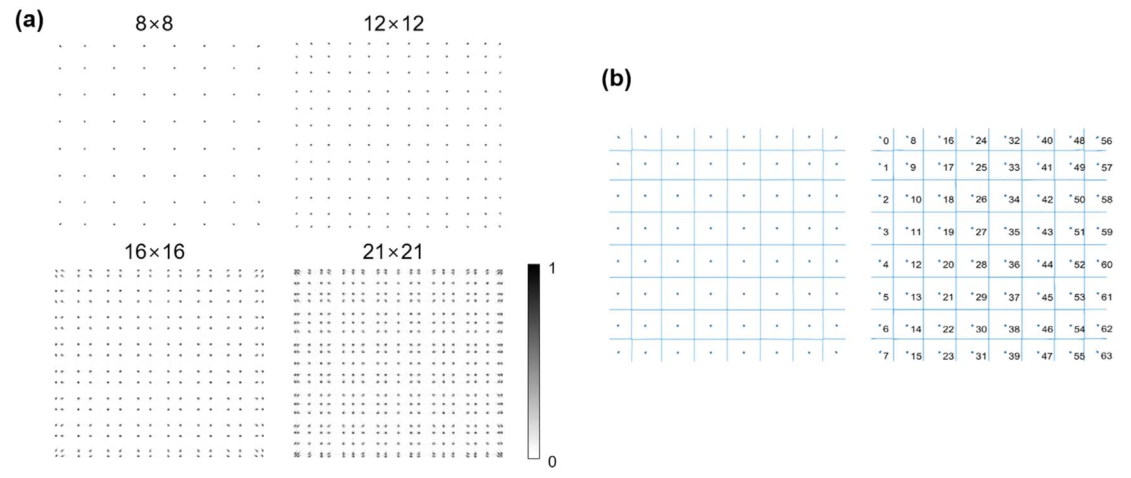

Figure 3. Illustrations of the process applying practical floodmap-based crystal assignment without any ICS recovery. (a) Floodmaps of 8×8, 12×12, 16×16, and 21×21 arrays generated by weighting the sensor positions with respective signal amplitudes. (b) To emulate a configuration without ICS recovery, a Voronoi diagram based on the peaks on the floodmap was drawn (blue solid line), and the segmented areas were indexed in order (numbers on the map). For each acquired event, the index of the segment to which a weighted position belonged was assigned as the interacted crystal.

$$\text{PE:} \quad \frac{\#(\text{Crystal with } E_1 = \text{Interacted crystal})}{\#(\text{Total PE events})} \times 100\%$$

$$\text{ICS:} \quad \frac{\#(\text{Crystals with } E_1 \text{ and } E_2 = \text{Interacted crystals})}{\#(\text{Total ICS events})} \times 100\%.$$

After applying ICS-eNet to the test dataset, we investigated the linearity between the true and estimated E_1 and E_2 values of the ICS events. For each linear fitting, R^2 value was measured to evaluate the energy estimation accuracy.

2.4.1.1. Comparison with the convex optimization method

The ICS identification performance of ICS-eNet was compared with that of an existing convex (CVX) constrained optimization method (Lee *et al* 2018). In the CVX method, the relationship between the energy deposition ratios in N^2 crystals (x) and M^2 photosensor responses (y) is assumed to be linear based on a pre-calculated $N^2 \times M^2$ matrix (A) of the characteristic photosensor response for PE event on each crystal as follows:

$$y = Ax, \quad \sum x = 1.$$

The CVX method finds a positive $N^2 \times 1$ solution x by minimizing $\|y - Ax\|_2$, which corresponds to the $N \times N$ output of ICS-eNet. The CVX method was applied to the same dataset using Matlab-based CVX program (Grant and Boyd 2013) for each detector design. After applying the same E_1/E_2 algorithm to vector x, the event classification accuracy, crystal selection accuracy, and energy linearity were evaluated as described in section 2.4.1.

2.4.2. ICS-cNet

The performance of ICS-cNet was evaluated according to the crystal selection accuracy, RMSE distance, and relative RMSE distance reduction. The crystal selection accuracy of ICS-cNet was defined as the percentage of events in which ICS-cNet accurately selected the first-interacted crystal. As a metric representing the point spread, we measured the RMSE of the 2D distance between the centers of the predicted and true first-interacted crystals. Additionally, the relative RMSE distance reduction was used as a metric to indirectly evaluate the effect of the ICS recovery on the spatial resolution relative to the crystal pitch as follows:

$$\frac{\text{RMSE distance}_{No\ recovery}[\text{mm}] - \text{RMSE distance}_{ICS-cNet}\ [\text{mm}]}{\text{Crystal pitch [mm]}}.$$

Here, the term *No recovery* corresponds to the configuration emulated by conducting a typically used floodmap-based crystal assignment to evaluate the impact of ICS-cNet on the performance compared to the case without the ICS recovery. From the simulation data, the floodmap was generated by weighting the sensor positions with respective signal amplitudes, which was analogous to Anger logic (figure 3). Because the peaks represent the photon interactions in the individual crystals, the floodmap was partitioned by drawing a Voronoi

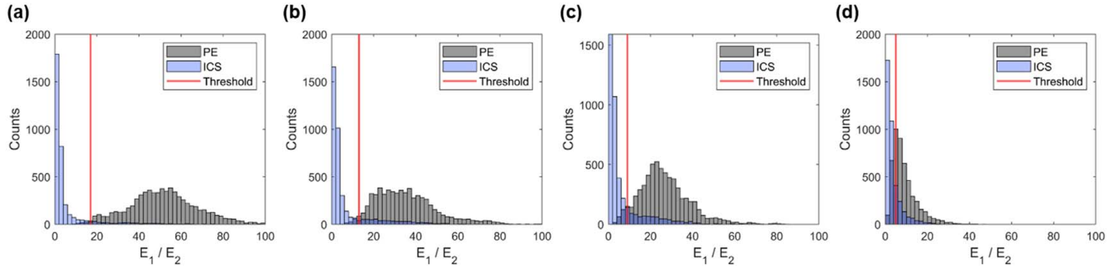

Figure 4. Histograms of E_1/E_2 estimated by ICS-eNet for PE and ICS events in (a) 8 × 8, (b) 12 × 12, (c) 16 × 16, and (d) 21 × 21 arrays. The red vertical lines indicate the threshold set to classify the event as PE or ICS.

Table 2. Occurrence rates of PE and ICS events among all events [%].

		8 × 8	12 × 12	16 × 16	21 × 21
PE (#Crystal = 1)		66.3	60.8	58.1	56.5
ICS	#Crystal = 2	28.6	31.8	33.0	33.5
	#Crystal = 3	4.7	6.6	7.9	8.5
	#Crystal > 3	0.4	0.8	1.2	1.4

diagram of the peak positions. The interacted crystal of each event was assigned as the index corresponding to the partition to which the event point on the floodmap belonged.

2.5. Spatial resolution

To measure the spatial resolution, we simulated a point source in PET rings comprising the detector blocks described in section 2.1. The ring consisted of 18 transaxial and 1 axial detector blocks with an inner diameter of 170 mm. To combine the effects of acolinearity and positron range, we used a spherical source with a radius of 0.25 mm, which was placed at the center of a 10 mm plastic cube, emitting positrons with an energy distribution identical to ^{18}F. The source was placed at the center of the field-of-view and 4 cm off-center in the radial direction.

We applied three different methods to the acquired coincidence datasets: ICS-eNet with proportional scheme, ICS-cNet, and floodmap-based crystal assignment. The proportional scheme weighted the recorded ICS events proportionally to the number of recorded PE events after the events were classified as PE or ICS by ICS-eNet. The details of applying this scheme for ICS were described in a previous work (Lee *et al* 2020). Assuming that one photon underwent PE in crystal P_A of detector A and another photon underwent ICS in crystals S_{B1} and S_{B2} of detector B, the numbers of LORs for P_AS_{B1} and P_AS_{B2} were given as follows:

$$\mathrm{LOR}_{P_A S_{Bu}} = \mathrm{PE}_{P_A S_{Bu}} + \frac{\mathrm{PE}_{P_A S_{Bu}}}{\mathrm{PE}_{P_A S_{B1}} + \mathrm{PE}_{P_A S_{B2}}} \mathrm{ICS}_{P_A S_{B1} S_{B2}} \text{ for } u \in \{1, 2\},$$

where the subscripts denote the interacted crystals in PE or ICS events.

Similarly, in the case where both annihilation photons underwent ICS (one in the crystals S_{A1} and S_{A2}, and another in S_{B1} and S_{B2}), the numbers of LORs were given as follows:

$$\mathrm{LOR}_{S_{Au} S_{Bv}} = \mathrm{PE}_{S_{Au} S_{Bv}} + \frac{\mathrm{PE}_{S_{Au} S_{Bv}}}{\mathrm{PE}_{S_{A1} S_{B1}} + \mathrm{PE}_{S_{A1} S_{B2}} + \mathrm{PE}_{S_{A2} S_{B1}} + \mathrm{PE}_{S_{A2} S_{B2}}} \mathrm{ICS}_{S_{A1} S_{A2} S_{B1} S_{B2}} \text{for } u \in \{1, 2\}$$

and $v \in \{1, 2\}$.

For each configuration, the image of the point source was reconstructed using 3D ordered-subset expectation maximization with 18 subsets and 1 iteration in common. The length of the cubic image voxel was identical to half of the crystal pitch. We measured full width at half maximum (FWHM) resolutions based on the line profiles along radial, tangential, and axial directions. We also reported the improvements of the FWHM resolutions achieved by applying ICS-eNet or ICS-cNet compared with the case of no recovery:

$$\text{Improvement [\%]} = \frac{\mathrm{FWHM}_{No\ recovery} - \mathrm{FWHM}_{ICS-Net}}{\mathrm{FWHM}_{No\ recovery}}.$$

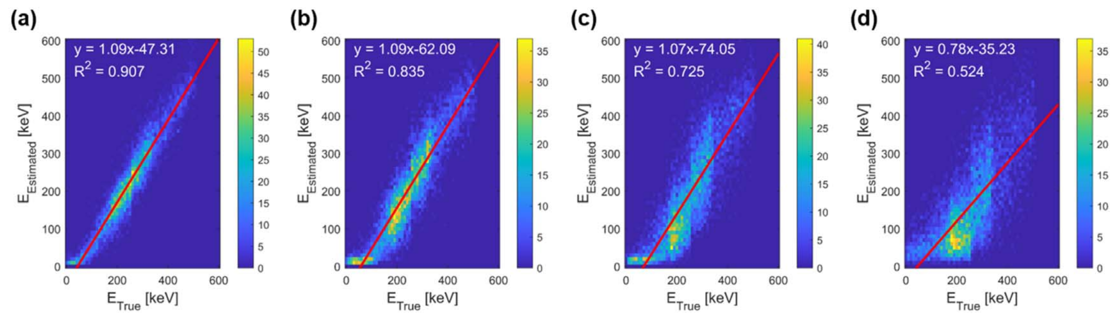

Figure 5. 2D histograms of true versus estimated energies for ICS-eNet and the linear fittings of (a) 8 × 8, (b) 12 × 12, (c) 16 × 16, and (d) 21 × 21 arrays.

Table 3. Event classification and crystal selection accuracy of ICS-eNet.

		8 × 8		12 × 12		16 × 16		21 × 21	
		ICS-eNet	CVX	ICS-eNet	CVX	ICS-eNet	CVX	ICS-eNet	CVX
Event classification accuracy [%]		97	97	92	93	90	80	77	65
Crystal selection accuracy [%]	PE	99	100	98	100	95	89	75	67
	ICS	91	96	78	85	62	57	35	25

3. Results

3.1. Occurrence rates

The occurrence of ICS was more significant in higher-CSR detectors (table 2). In low-CSR detectors with a large crystal pitch, the remaining energy was deposited before the scattered annihilation photons exited the first crystal to the adjacent crystals. Because the proportions of the events in which three or more crystals interacted were <10% for all the detectors, we could justify the selection of only two crystals of ICS events to simplify the recovery with ICS-eNet, neglecting further scatterings.

3.2. ICS-eNet

3.2.1. Event classification accuracy and crystal selection accuracy

As shown in figure 4, the E_1/E_2 distributions of the PE and ICS events were clearly separated in the low-CSR detectors. This indicates that the threshold can be easily determined at the local minima of the mixed histogram in reality. As the CSR increased, the E_1/E_2 values of PE decreased and the area of overlap between the PE and ICS increased. The event classification accuracy remained at 90% up to the 16 × 16 array. However, performance degradation was observed for the 21 × 21 array (table 3). Selecting one interacted crystal of the PE events was highly accurate for the 8 × 8, 12 × 12, and 16 × 16 arrays. However, for the ICS events, the crystal selection accuracy decreased significantly as the CSR increased. Note that the crystal selection for the ICS events was considered correct when both interacted crystals were accurately determined.

As indicated by the floodmaps in figure 3, the limitation of ICS-eNet in the high CSR detectors resulted from the highly superposed ICS energy information from the crystals to the signal distributions. Because each sensor covered numerous crystals, the response of the signal distribution was insensitive to different amounts of energy deposition. Therefore, the network was not trained to fully identify the differences in the signal distributions that were input to the network.

Compared with ICS-eNet, the CVX method exhibited higher crystal selection accuracies of ICS events for the 8 × 8 and 12 × 12 detectors, but lower accuracies for the 16 × 16 and 21 × 21 detectors (table 3). This degradation in the overall performance due to an increase in the CSR was more significant for CVX than for ICS-eNet. Applying CVX to a light-sharing detector is equivalent to solving an underdetermined system event-by-event; as CSR increases, a large number of variables (x) are determined by a limited number of observations (y) based on the characteristic matrix (A) generated by PE events, which yields noisy solutions. In contrast, ICS-eNet yielded relatively small degradation under high CSR conditions, owing to sufficient hidden units trained with abundant combinations of crystal interactions, indicating that ICS-eNet is more suitable than CVX for high-resolution detectors.

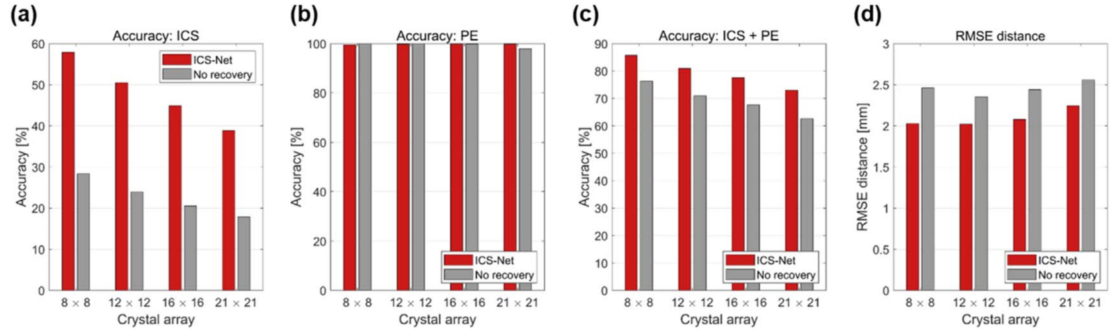

Figure 6. Performance of ICS-cNet compared with the case without recovery. (a)–(c) Accuracies of selecting the first-interacted crystals of (a) ICS, (b) PE, and (c) ICS + PE events. (d) RMSE distance of the 2D crystal position predicted by ICS-cNet.

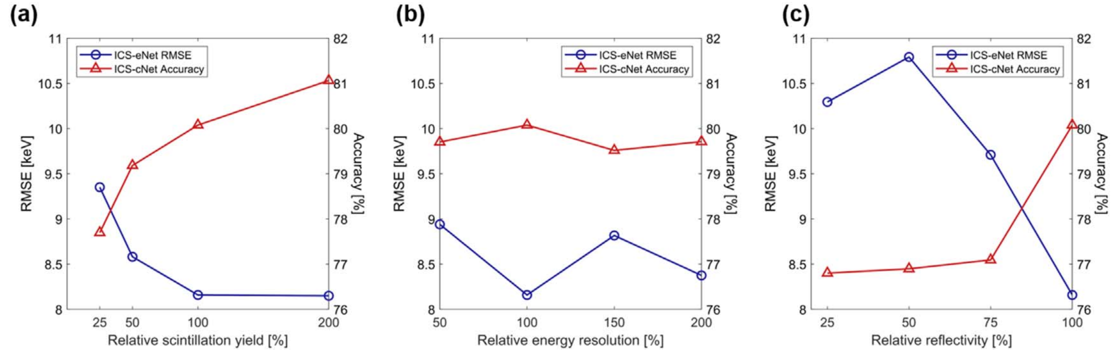

Figure 7. Effects of the (a) scintillation yield, (b) energy resolution, and (c) crystal reflectivity on the ICS-eNet RMSE and ICS-cNet accuracy. The 100% relative value indicates the default setting used throughout the study.

Table 4. Comparison of fitted lines and R^2 values between ICS-eNet and CVX for estimating E_1 and E_2.

	Fitted line		R^2	
	ICS-eNet	CVX	ICS-eNet	CVX
8 × 8	$y = 1.09x - 47.31$	$y = 1.14x - 48.43$	0.907	0.913
12 × 12	$y = 1.09x - 62.09$	$y = 1.14x - 64.05$	0.835	0.806
16 × 16	$y = 1.07x - 74.05$	$y = 1.07x - 63.56$	0.725	0.662
21 × 21	$y = 0.78x - 35.23$	$y = 0.79x - 17.94$	0.524	0.390

3.2.2. Energy linearity

The relationships between the true and estimated energies of the ICS events are demonstrated in figure 5. For low-CSR detectors, ICS-eNet yielded strong correlations, with slope values approximately equal to 1. The 21 × 21 array exhibited poor energy linearity and a small slope value because the signal distributions could not fully reflect the energy deposition pattern. Most events with $E_{\mathrm{Estimated}} < 50$ keV were ICS events that were misclassified into PE, implying that the event classification accuracy was affected by energy correlations.

Table 4 presents a comparison of the energy linearity performance between ICS-eNet and CVX. Again, ICS-eNet outperformed CVX in the accuracy of estimating E_1 and E_2 particularly for high-CSR detectors. The slope and bias values of the fitted lines for both methods were comparable.

3.3. ICS-cNet

3.3.1. Crystal selection accuracy

For all the detectors, the accuracy of ICS-cNet in selecting the first-interacted crystal of the ICS events was approximately twice that for the method with no recovery (figure 6(a)). The accuracy of selecting the crystal of the PE events was nearly 100% for all configurations (figure 6(b)). For the case of the 21 × 21 array with no

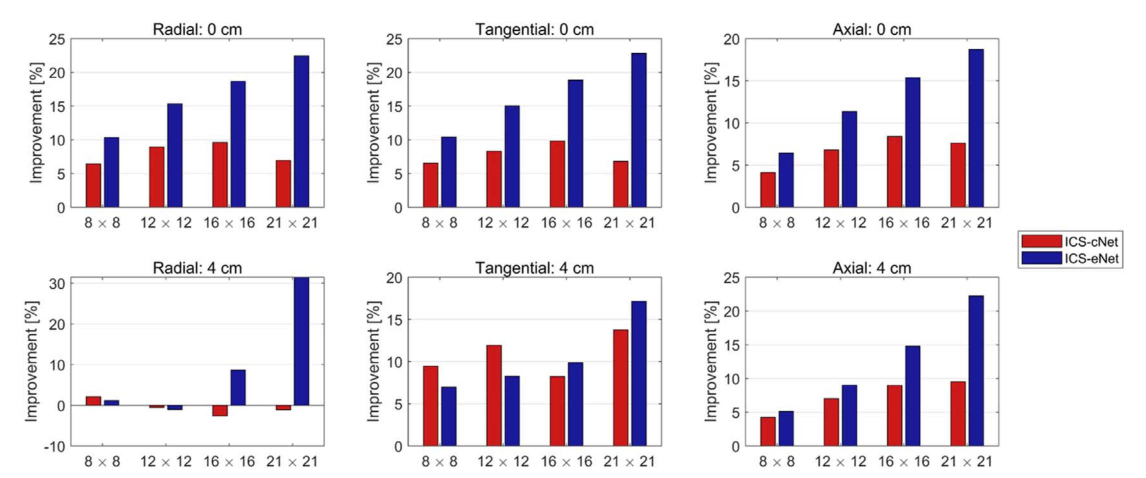

Figure 8. Improvements in the radial (left), tangential (middle), and axial (right) FWHM resolutions of the PET prototype achieved by applying ICS-cNet or ICS-eNet compared with the case without recovery. The radial offsets of the ^{18}F point source were 0 cm (upper) and 4 cm (lower).

Table 5. Relative RMSE distance reduction with the application of ICS-cNet.

8 × 8	12 × 12	16 × 16	21 × 21
0.135	0.132	0.225	0.262

recovery, the accuracy was slightly reduced owing to ambiguous boundaries between the edge crystals, as shown in figure 3(a). Combining the ICS and PE events, ICS-cNet achieved an accuracy improvement of >10% in selecting the first-interacted crystal, owing to the considerable increase in the crystal selection accuracy of the ICS events (figure 6(c)).

3.3.2. Error distance

In addition to its high accuracy, ICS-cNet reduced the RMSE distance compared with the case of no recovery for all the detectors (figure 6(d)). The absolute reduction of the RMSE distance due to application of ICS-cNet was more significant for the lower-CSR detectors, owing to the higher crystal selection accuracy and larger crystal pitch, although the ICS occurrence was less frequent as reported in section 3.1.

However, as shown in table 5, the relative reduction in the RMSE distance was more significant for higher-CSR detectors. This implies that, given the linear relationship between the spatial resolution and the crystal pitch, the impact of ICS-cNet is more significant in PET systems that require a high spatial resolution.

3.4. Effects of optical properties

Figure 7 shows the effects of the light yield, intrinsic energy resolution, and crystal reflectivity on the performance of the networks. To simplify the comparison of ICS-eNet, we reported the RMSE loss of estimating the energy deposition of the individual crystal, which is directly linked to the metrics described in sections 2.4.1 and 3.2. For ICS-cNet, we reported the accuracy of selecting the first-interacted crystal for the overall events (i.e. ICS + PE) as mentioned in sections 2.4.2 and 3.3.1.

The networks exhibited robust performance, varying within a few keV of the ICS-eNet RMSE and a few percentage points of the ICS-cNet accuracy under our simulation conditions. Slight dependencies on the scintillation yield and crystal surface reflectivity were observed. A high scintillation yield improved the statistical signal-to-noise level of the photosensor readout. This indicates that a high photosensor gain and bright scintillator are advantageous for applying the networks. The high reflectivity of the crystal elements efficiently discriminated the signals from the individual crystal in ICS events by constricting the scintillation dispersions. The effect of the intrinsic energy resolution was insignificant because the networks performed event-by-event normalization of the signal amplitude arrays.

3.5. Spatial resolution

Both networks improved the spatial resolution of the PET prototype compared with the case of no recovery (table 6 and figure 8). Applying ICS-eNet with the proportional scheme yielded a larger improvement than ICS-

Table 6. Radial, tangential, and axial FWHM resolutions of the prototype PET ring composed of each detector design. The radial offsets of the ^{18}F point source were 0 and 4 cm.

		8 × 8		12 × 12		16 × 16		21 × 21	
Radial offset		0 cm	4 cm	0 cm	4 cm	0 cm	4 cm	0 cm	4 cm
Radial	ICS-cNet	1.76	5.83	1.28	5.94	1.08	5.03	0.88	3.08
	ICS-eNet	1.69	5.89	1.19	5.98	0.97	4.48	0.73	2.09
	No recovery	1.88	5.96	1.40	5.91	1.19	4.90	0.94	3.05
Tangential	ICS-cNet	1.76	2.30	1.28	2.13	1.08	1.49	0.88	1.19
	ICS-eNet	1.68	2.36	1.19	2.22	0.97	1.46	0.73	1.14
	No recovery	1.88	2.54	1.40	2.42	1.19	1.62	0.95	1.38
Axial	ICS-cNet	1.66	1.66	1.15	1.13	0.94	0.92	0.76	0.76
	ICS-eNet	1.62	1.64	1.09	1.11	0.87	0.86	0.67	0.65
	No recovery	1.73	1.73	1.23	1.22	1.03	1.01	0.83	0.84

cNet in most cases. Although the results in section 3.2 indicated a low accuracy for hig- CSR detectors, ICS-eNet alleviated the ICS blurring in the images. ICS-cNet exhibited a similar tendency of a larger improvement for the high-CSR detector, as predicted from section 3.3.2. The impact of the networks was the smallest in the radial direction at a 4 cm offset where the parallax error of depth-of-interaction was dominant compared with the ICS blurring. However, ICS-eNet still achieved improvements in the 16 × 16 and 21 × 21 arrays.

4. Discussion

In this study, we designed and evaluated two different CNNs with different purposes. ICS-eNet was designed to identify the photon interactions and serve as a preprocessor before the application of existing ICS recovery algorithms. The first function of ICS-eNet is to classify each event as PE or ICS according to the ratio between the largest and second-largest energy outputs. The results presented in section 3.1 imply that the recovery process can be simplified without significantly affecting the accuracy by neglecting events with two or more Compton scattering. The second function is to select the interacted crystals and estimate the respective energy depositions. The slopes of the fitted lines in the distributions of true versus estimated energies were nearly 1 for the arrays up to 16 × 16. This indicates that no additional energy calibration was required. Because the R^2 value is directly linked to the uncertainty of the energy information, the use of ICS-eNet on the detectors up to the 16 × 16 arrays can increase the accuracy of the ICS recovery algorithms that employ the energy information. Although significant biases were introduced in the linear fitting, they could be corrected because the total energy was calibrated by the 511 keV peak from the detector block-level energy histogram.

Accurate information on the interaction positions and energies estimated by ICS-eNet can improve the performance of the ICS recovery algorithms proposed in previous studies. The ICS recovery algorithms include comparing the amount of energy (Comanor *et al* 1996, Shao *et al* 1996, Surti and Karp 2018), using Compton kinematics or Klein–Nishina cross-sections (Rafecas *et al* 2003, Pratx and Levin 2009, Abbaszadeh *et al* 2018), applying neural networks to LORs (Gillam *et al* 2014), and weighting the ICS events proportionally to the number of PEs (Lage *et al* 2015, Lee *et al* 2020). Our previous studies focused on the proportional weighting scheme because it significantly improved the image quality and had the advantage that selecting two interacted crystals is enough to recover ICS, without the use of energy information (Lee *et al* 2018, 2020). The proportional scheme consistently yielded good performance in combination with ICS-eNet in this study, improving spatial resolution of the PET ring. Although ICS-eNet exhibited poor accuracy and energy linearity for high CSR, the impact was minimized because the proportional scheme requires energy estimations only for classifying the events, not for directly finding the first-interacted crystal.

ICS-cNet was proposed to simplify the recovery steps by directly selecting the first-interacted crystal. Existing ICS recovery algorithms use explicit modeling of Compton scattering physics or maximum likelihood. The most significant advantage of ICS-cNet is its simplicity when integrating the entire inference process based solely on data measurements. As mentioned in section 3.3, ICS-cNet exhibited satisfactory performance regardless of the CSR. The significant relative RMSE distance reduction in high-CSR detectors highlights the importance of ICS-cNet application in high-resolution PET systems. Along with this result, ICS-cNet improved the spatial resolution for high CSR detectors. Additionally, ICS-cNet alleviated the impact of ICS on the spatial resolution of low CSR detectors owing to its high recovery accuracy and large crystal pitch.

For training ICS-cNet in reality, several possible methods can be used to accurately identify the first-interacted crystals. For example, a lead collimator with thin wells can be used to control the direction of irradiation to each crystal. Mechanical collimators are widely employed for calibrating the interaction positions within detectors using monolithic crystals (Bruyndonckx *et al* 2006, Maas *et al* 2009, Marcinkowski *et al* 2016, Peng *et al* 2019). Another option is electronic collimation by acquiring coincidence events between the test detector and a small single reference detector. To irradiate every crystal with a narrow beam width, the point source is placed directly in front of the top face of the target crystal while the reference detector is placed at a distance from the crystal and aligned perpendicularly to the crystal. Strategies for accelerating the tasks will be developed for practical applications at the system level.

Training ICS-eNet is challenging because the exact energy depositions are unknown. A possible approach is to transfer the network trained by the Monte Carlo simulation to actual data. Additional data, such as a floodmap, can be utilized as the network input to train the characteristics of the real detector response. One paper proposed the implementation of a network ensemble which exhibits good performance in applying networks trained by simulation-only data to real detectors (Iborra *et al* 2019). Methodologies for the efficient training of ICS-eNet will be further developed.

Our proof-of-concept study demonstrates the potential of CNNs for ICS recovery in light-sharing PET detectors. The simple CNN structures learned the patterns of the ICS events to estimate the energy depositions and the first-interacted crystals, and achieved adequate performance for a wide range of CSRs. Metrics such as crystal selection accuracy and energy linearity were used in this study to indirectly assess the impact of the proposed method on the PET image quality. The enhanced spatial resolution with ICS recovery is expected to improve the contrast and the lesion detectability of the reconstructed PET images.

The final goal of this study is to achieve high resolution in real PET imaging by alleviating the ICS effect on blurring with the proposed methods. The methodology for experimental training of the networks will be first established to be practically implementable in the scanner construction. Along with further improvement of the network accuracy, various phantom imaging will be conducted with a PET ring constructed by the trained detectors. ICS effect depends on the aspect ratio of the crystal elements and capability of measuring depth-of-interaction because ICS effect is combined with other detector blurring factors such as parallax error and crystal penetration (Rahmim *et al* 2013). In section 3.5, ICS recovery exhibited limited improvements in radial resolution where parallax error is dominant. A systematic study will be designed to quantify the impact of each blurring factor and to improve accuracy of point spread function modeling.

5. Conclusion

In this study, we assessed the feasibility and performance of CNN-based ICS recovery methods for PET detectors with various light-sharing designs. The results indicate that ICS-eNet accurately identified ICS events and estimated the energy depositions, while ICS-cNet achieved suitable accuracy in selecting the first-interacted crystals and reduced the error distance for all the detectors. Both networks enhanced the spatial resolution of the PET ring, particularly for highly pixelated arrays. The proposed CNN models are expected to recover ICS effectively and improve the overall image quality of PET using light-sharing detector designs.

Acknowledgments

This work was supported by grants from the National Research Foundation of Korea (NRF) funded by the Korean Ministry of Science and ICT (Grant No. NRF-2016R1A2B3014645).

ORCID iDs

Jae Sung Lee https://orcid.org/0000-0001-7623-053X

References

Abbaszadeh S, Chinn G and Levin C S 2018 Positioning true coincidences that undergo inter-and intra-crystal scatter for a sub-mm resolution cadmium zinc telluride-based PET system *Phys. Med. Biol.* **63** 025012

Akamatsu G *et al* 2019 Performance evaluation of a whole-body prototype PET scanner with four-layer DOI detectors *Phys. Med. Biol.* **64** 095014

Ametamey S M, Honer M and Schubiger P A 2008 Molecular imaging with PET *Chem. Rev.* **108** 1501–16

Berger M J, Hubbell J H, Seltzer S M, Chang J, Coursey J S, Sukumar R, Zucker D S and Olsen K 2010 XCOM: Photon cross sections database (https://doi.org/10.18434/T48G6X)

Borghi G, Tabacchini V, Bakker R and Schaart D R 2018 Sub-3 mm, near-200 ps TOF/DOI-PET imaging with monolithic scintillator detectors in a 70 cm diameter tomographic setup *Phys. Med. Biol.* **63** 155006

Bruyndonckx P, Léonard S, Lemaître C, Tavernier S and Wu Y 2006 Performance study of a PET detector module based on a continuous scintillator *IEEE Trans. Nucl. Sci.* **53** 2536–42

Cherry S R, Jones T, Karp J S, Qi J, Moses W W and Badawi R D 2018 Total-body PET: Maximizing sensitivity to create new opportunities for clinical research and patient care *J. Nucl. Med.* **59** 3–12

Comanor K A, Virador P R G and Moses W W 1996 Algorithms to identify detector compton scatter in pet modules *IEEE Trans. Nucl. Sci.* **43** 2213–8

Du J, Schmall J P, Yang Y, Di K, Dokhale P A, Shah K S and Cherry S R 2013 A simple capacitive charge-division readout for position-sensitive solid-state photomultiplier arrays *IEEE Trans. Nucl. Sci.* **60** 3188–97

Gillam J E, Solevi P, Oliver J F, Casella C, Heller M, Joram C and Rafecas M 2014 Sensitivity recovery for the AX-PET prototype using inter-crystal scattering events *Phys. Med. Biol.* **59** 4065–83

Gong K, Berg E, Cherry S R and Qi J 2020 Machine learning in PET: from photon detection to quantitative image reconstruction *Proc. IEEE* **108** 51–68

Gonzalez-Montoro A *et al* 2017 Performance study of a large monolithic LYSO PET detector with accurate photon DOI using retroreflector layers *IEEE Trans. Radiat. Plasma Med. Sci.* **1** 229–37

Grant A M, Deller T W, Khalighi M M, Maramraju S H, Delso G and Levin C S 2016 NEMA NU 2-2012 performance studies for the SiPM-based ToF-PET component of the GE SIGNA PET/MR system *Med. Phys.* **43** 2334–43

Grant M and Boyd S 2013 CVX: Matlab software for disciplined convex programming, version 2.0 beta [WWW Document]. URL (http://cvxr.com/cvx)

Hegazy M A A, Cho M H, Cho M H and Lee S Y 2019 U-net based metal segmentation on projection domain for metal artifact reduction in dental CT *Biomed. Eng. Lett.* **9** 375–85

Hsu D F C, Freese D L, Innes D R and Levin C S 2019 Intercrystal scatter studies for a 1 mm^3 resolution clinical PET system prototype *Phys. Med. Biol.* **64** 090524

Hwang D, Kim K Y, Kang S K, Seo S, Paeng J C, Lee D S and Lee J S 2018 Improving the accuracy of simultaneously reconstructed activity and attenuation maps using deep learning *J. Nucl. Med.* **59** 1624–9

Iborra A, González A J, González-Montoro A, Bousse A and Visvikis D 2019 Ensemble of neural networks for 3D position estimation in monolithic PET detectors *Phys. Med. Biol.* **64** 195010

Ito M, Hong S J and Lee J S 2011 Positron emission tomography (PET) detectors with depth-of- interaction (DOI) capability *Biomed. Eng. Lett.* **1** 70–81

Ito M, Lee M S and Lee J S 2013 Continuous depth-of-interaction measurement in a single-layer pixelated crystal array using a single-ended readout *Phys. Med. Biol.* **58** 1269–82

Jan S *et al* 2004 GATE: a simulation toolkit for PET and SPECT *Phys. Med. Biol.* **49** 4543–61

Khouani A, El Habib Daho M, Mahmoudi S A, Chikh M A and Benzineb B 2020 Automated recognition of white blood cells using deep learning *Biomed. Eng. Lett.* **10** 359–67

Ko G B, Yoon H S, Kwon S I, Lee C M, Ito M, Hong S J, Lee D S and Lee J S 2013 Development of a front-end analog circuit for multi-channel SiPM readout and performance verification for various PET detector designs *Nucl. Instrum. Methods Phys. Res.* A **703** 38–44

Krishnamoorthy S, Blankemeyer E, Mollet P, Surti S, Van Holen R and Karp J S 2018 Performance evaluation of the MOLECUBES β-CUBE - a high spatial resolution and high sensitivity small animal PET scanner utilizing monolithic LYSO scintillation detectors *Phys. Med. Biol.* **63** 155013

Kwon S I *et al* 2011 Development of small-animal PET prototype using silicon photomultiplier (SiPM): initial results of phantom and animal imaging studies *J. Nucl. Med.* **52** 572–9

Lage E, Parot V, Moore S C, Sitek A, Udías J M, Dave S R, Park M-A, Vaquero J J and Herraiz J L 2015 Recovery and normalization of triple coincidences in PET *Med. Phys.* **42** 1398–410

Lecun Y, Bengio Y and Hinton G 2015 Deep learning *Nature* **521** 436–44

Lee J S 2020 A review of deep learning-based approaches for attenuation correction in positron emission tomography *IEEE Trans. Radiat. Plasma Med. Sci.* **5** 160–84

Lee M S, Hwang D, Kim J H and Lee J S 2019 Deep-dose: a voxel dose estimation method using deep convolutional neural network for personalized internal dosimetry *Sci. Rep.* **9** 1–9

Lee M S, Kang S K and Lee J S 2018 Novel inter-crystal scattering event identification method for PET detectors *Phys. Med. Biol.* **63** 115015

Lee M S, Kim K Y, Ko G B and Lee J S 2017 Prototype pre-clinical PET scanner with depth-of-interaction measurements using single-layer crystal array and single-ended readout *Phys. Med. Biol.* **62** 3983–96

Lee S, Kim K Y, Lee M S and Lee J S 2020 Recovery of inter-detector and inter-crystal scattering in brain PET based on LSO and GAGG crystals *Phys. Med. Biol.* **65** 195005

Lee S, Lee M S, Kim K Y and Lee J S 2018 Systematic study on factors influencing the performance of interdetector scatter recovery in small-animal PET *Med. Phys.* **45** 3551–62

Levin A and Moisan C 1996 More physical approach to model the surface treatment of scintillation counters and its implementation into DETECT *IEEE Nucl. Sci. Symp. Med. Imaging Conf.* Vol 2 *(Anaheim, CA, 2-9 November 1996)* (Picastaway, NJ: IEEE) 702–6

Maas M C, Schaart D R, Van Der Laan D J, Bruyndonckx P, Lematre C, Beekman F J and Van Eijk C W E 2009 Monolithic scintillator PET detectors with intrinsic depth-of-interaction correction *Phys. Med. Biol.* **54** 1893–908

Marcinkowski R, Mollet P, Van Holen R and Vandenberghe S 2016 Sub-millimetre DOI detector based on monolithic LYSO and digital SiPM for a dedicated small-animal PET system *Phys. Med. Biol.* **61** 2196–212

Miyaoka R S and Lewellen T K 2000 Effect of detector scatter on the decoding accuracy of a DOI detector module *IEEE Trans. Nucl. Sci.* **47** 1614–9

Ota R, Omura T, Yamada R, Miwa T and Watanabe M 2016 Evaluation of a sub-millimeter resolution PET detector with a 1.2 mm Pitch TSV-MPPC array one-to-one coupled to LFS scintillator crystals and inter-crystal scatter studies with individual signal readout *IEEE Trans. Radiat. Plasma Med. Sci.* **1** 15–22

Park H, Ko G B and Lee J S 2017 Hybrid charge division multiplexing method for silicon photomultiplier based PET detectors *Phys. Med. Biol.* **62** 4390–405

Park H and Lee J S 2020 SiPM signal readout for inter-crystal scatter event identification in PET detectors *Phys. Med. Biol.* **65** 205010

Park J, Hwang D, Kim K Y, Kang S K, Kim Y K and Lee J S 2018 Computed tomography super-resolution using deep convolutional neural network *Phys. Med. Biol.* **63** 145011

Peng P, Judenhofer M S and Cherry S R 2019 Compton PET: a layered structure PET detector with high performance *Phys. Med. Biol.* **64** 10LT01

Phelps M E 2000 Positron emission tomography provides molecular imaging of biological processes *Proc. Natl. Acad. Sci. USA* **97** 9226–33

Pratx G and Levin C S 2009 Bayesian reconstruction of photon interaction sequences for high-resolution PET detectors *Phys. Med. Biol.* **54** 5073–94

Rafecas M, Böning G, Pichler B J, Lorenz E, Schwaiger M and Ziegler S I 2003 Inter-crystal scatter in a dual layer, high resolution LSO-APD positron emission tomograph *Phys. Med. Biol.* **48** 821–48

Rahmim A, Qi J and Sossi V 2013 Resolution modeling in PET imaging: theory, practice, benefits, and pitfalls *Med. Phys.* **40** 064301

Ritzer C, Hallen P, Schug D and Schulz V 2017 Intercrystal scatter rejection for pixelated PET detectors *IEEE Trans. Radiat. Plasma Med. Sci.* **1** 191–200

Schmidt F P, Kolb A and Pichler B J 2018 Optimization, evaluation and calibration of a cross-strip DOI detector *Phys. Med. Biol.* **63** 045022

Shao Y, Cherry S R, Siegel S and Silverman R W 1996 A study of inter-crystal scatter in small scintillator arrays designed for high resolution PET imaging *IEEE Trans. Nucl. Sci.* **43** 1938–44

Son J-W, Kim K Y, Park J Y, Kim K, Lee Y S, Ko G B and Lee J S 2020 SimPET: a preclinical PET insert for simultaneous PET/MR imaging *Mol. Imaging Biol.* **22** 1208–17

Surti S and Karp J S 2018 Impact of event positioning algorithm on performance of a whole-body PET scanner using one-to-one coupled detectors *Phys. Med. Biol.* **63** 055008

Teimoorisichani M and Goertzen A L 2019 A study of inter-crystal scatter in dual-layer offset scintillator arrays for brain-dedicated PET scanners *Phys. Med. Biol.* **64** 115007

Van Sluis J, De Jong J, Schaar J, Noordzij W, Van Snick P, Dierckx R, Borra R, Willemsen A and Boellaard R 2019 Performance characteristics of the digital biograph vision PET/CT system *J. Nucl. Med.* **60** 1031–6

Yamamoto S and Ishibashi H 1998 A GSO depth of interaction detector for PET *IEEE Trans. Nucl. Sci.* **45** 1078–82

Yoon H S, Ko G B, Kwon S I, Lee C M, Ito M, Song I C, Lee D S, Hong S J and Lee J S 2012 Initial results of simultaneous PET/MRI experiments with an MRI-compatible silicon photomultiplier PET scanner *J. Nucl. Med.* **53** 608–14

Zhang C, Sang Z, Wang X, Zhang X and Yang Y 2019 The effects of inter-crystal scattering events on the performance of PET detectors *Phys. Med. Biol.* **64** 205004